

Characterizing the Deep Pumping-induced Subsidence Against Metro Tunnel Using Vertically Distributed Fiber-Optic Sensing

Yunxiao Xin

Nanjing University

Xiaozhao Li (✉ hapoaaa@foxmail.com)

Nanjing University <https://orcid.org/0000-0002-7049-8989>

Wei Zhang

Nanjing University

Qi Wang

Geo-engineering Investigation Institute of Jiangsu Province

Research Article

Keywords: Deep pumping, Differential settlement, Metro tunnel, Distributed fiber-optic sensing (DFOS), Space-time matrix

Posted Date: March 17th, 2021

DOI: <https://doi.org/10.21203/rs.3.rs-168411/v1>

License:   This work is licensed under a Creative Commons Attribution 4.0 International License.

[Read Full License](#)

Version of Record: A version of this preprint was published at Environmental Earth Sciences on November 1st, 2021. See the published version at <https://doi.org/10.1007/s12665-021-09990-z>.

Characterizing the deep pumping-induced subsidence against metro tunnel using vertically distributed fiber-optic sensing

Xin Yunxiao¹, Li Xiaozhao^{1*}, Zhang Wei¹, Wang Qi²

1. School of Earth Sciences and Engineering, Nanjing University, 163 Xianlin Avenue,
Nanjing, 210023, China
2. Geo-engineering Investigation Institution of Jiangsu Province, 17 Meilin Street, Nanjing,
211101, China

Corresponding Author:

Li Xiaozhao

Professor, Ph.D. supervisor, School of Earth Sciences and Engineering, Nanjing University,

No. 163 Xianlin Avenue, Nanjing, 210023, PR China

Email: lixz@nju.edu.cn

1 **Abstract:** Continuous pumping of groundwater will induce uneven ground settlement, which
2 may adversely affect the nearby metro tunnels. In this paper, taking Nantong Metro Line 1
3 crossing Nantong Port Water Plant as an example, the surface level measurement and
4 subsurface deformation monitoring using vertically distributed fiber-optic sensing are
5 implemented to acquire the surface and subsurface settlement of emergency water supply
6 conditions. The fiber optic cable vertically buried in the constant-temperature layer is used to
7 measure the subsurface strain field and deduce the deformation amount of each stratum. The
8 monitoring results show that, during the pumping, the deformation of the aquifer and ground
9 surface is linearly compressed with time; after the pumping, the ground surface continues to
10 settle linearly at a slower rate for about 50 days, followed by a slow linear rebound, and the
11 aquifer is logarithmically rebounded. In addition, deep pumping causes the deformation of the
12 aquifers to be much greater than the surface settlement; the surface settlement lags behind the
13 settlement of the aquifer by 1 to 2 months; the surface rebound recovery also exhibits a similar
14 delay. Fitting models were derived to predict the maximum settlement and curvature radius of
15 the site, which indicates that the adverse effects against the metro tunnel are not negligible once
16 the continuous pumping exceeds 15 days. Those insights can be referred by the practitioners
17 for the control of urban subsidence.

18 **Keywords:** Deep pumping; Differential settlement; Metro tunnel; Distributed fiber-optic
19 sensing (DFOS); Space-time matrix.

20

21 **1. INTRODUCTION**

22 Ground subsidence is a hazardous environmental geology issue which not only reduces
23 stratum elevations but also yields damage to buildings and infrastructure (Herrera-García et al.,
24 2021; Pacheco-Martínez et al., 2013). Moreover, for metro tunnels, one of the most common
25 linear underground infrastructures in cities, the longitudinal differential deformation induced
26 by ground subsidence can lower their safety, durability, and waterproof performances (Peng et
27 al., 2017; Wang et al., 2016). The variation of the groundwater level induced by human
28 activities is a major cause of differential subsidence in urban areas (Edalat et al., 2020; Xu et
29 al., 2016b; Xue et al., 2005). Particularly, for those cities which have to withdraw underground
30 water as the water supply, long-term pumping activities in the water source area might induce
31 serious subsidence problems (Chai et al., 2004; Othman and Abotalib, 2019).

32 Given the differential settlement, former studies mainly focused on its impacts on surface
33 buildings. However, recent studies of ground subsidence against metro tunnels have revealed
34 that, compared with the negative impacts imposed by the settlement of ground surface, those
35 induced by the subsurface deformation are more significant for underground infrastructures
36 (Shen et al., 2014). Zheng et al. (2014) studied the stratified settlement caused by the extraction
37 of confined water using field tests and found that the deformation of phreatic layers is less than
38 that of the confined aquifer layers, which was other than the acknowledged settlement law
39 caused by dewatering of ground surface. Note a growing consensus has suggested that ground
40 subsidence occurs lagging behind the pumping activity (Kearns et al., 2015), and the duration
41 of land subsidence induced by deep pumping is longer than that by surface pumping (Cui and

42 Jia, 2018). However, current theoretical models of the pumping-induced settlement remain
43 unavailable to fully characterize the abovementioned influencing factors (Budhu and Adiyaman,
44 2010; Wang et al., 2018; Xu et al., 2012; Zhang et al., 2017; Zhou et al., 2017). Therefore,
45 concerning extracting deep groundwater scenarios, current models still have to be deliberately
46 calibrated by the field measurements (Shen and Xu, 2011; Xu et al., 2016a).

47 As is known, the ground subsidence can be monitored by a variety of measures (Poland et
48 al., 2006), such as leveling (Abidin et al., 2001), GPS (Baldi et al., 2009; Choudhury et al.,
49 2018; Hu et al., 2006; Mousavi et al., 2001), InSAR (Calderhead et al., 2011; Motagh et al.,
50 2017), and their combinations (Galloway and Burbey, 2011; Saleh and Becker, 2018). Note all
51 those measures cannot acquire layered subsidence measurements; even the layered marks can
52 acquire, in that the layered settlement meters are fixed-point arranged, the discrete subsidence
53 measurements cannot finely characterize the subsurface deformation field (Jiang et al., 2016).
54 The distributed fiber-optic sensing (DFOS), a novel monitoring technique, can obtain the strain
55 field along the sensing cable. Although the DFOS has been employed to monitor the subsurface
56 deformation field of Shengze, an abnormal post-dewatering subsiding area in Suzhou of China
57 (Gu et al., 2018; Zhang et al., 2018), however, few works have been documented to use DFOS
58 to monitor the variation process of the subsurface deformation field during a rapid pumping,
59 no mention assess its negative impacts against metro tunnels.

60 In this paper, taking a groundwater plant near Nantong Port, Jiangsu Province of China, as
61 an example, a test of deep multi-well dewatering was implemented to verify the applicability
62 and feasibility of the DFOS technique to monitor the variation of the subsurface deformation

63 field. Feature extraction on the DFOS measurements was also performed to assess the impacts
64 of subsurface settlement against the metro tunnel. Fitting equations were deduced to shed light
65 on the evolutionary trend of the surface and subsurface deformation field during and after the
66 pumping, which can be used to predict its long-term impacts against the metro tunnel.

67 **2. PRINCIPLE OF DISTRIBUTED FIBER-OPTIC SENSING (DFOS)**

68 A variety of DFOSs can be used for strain field monitoring (Zhang et al., 2014). Typically,
69 the Brillouin optical time-domain reflectometer (BOTDR) is used in this paper. The principle
70 of the BOTDR is based on the change in the scattered light caused by nonlinear interactions
71 between the incident light and the phonons which are thermally excited within the light
72 propagation medium. When occurring in an optical fiber, the backscattered light experiences a
73 frequency shift (the Brillouin frequency), which is dependent on the temperature and strain
74 environment of the fiber (Wu et al., 2015). Compared with other scattered lights, a substantial
75 advantage of Brillouin scattering is that its frequency shift caused by temperature is only
76 0.002 %/°C, which is much smaller than that caused by strain. Therefore, while measuring the
77 Brillouin frequency shift induced by strain, the influence of the temperature on the Brillouin
78 frequency shift can be neglected if the changes of temperature are within 2 °C. The relationship
79 between the Brillouin frequency shift and the strain of optical fiber yields:

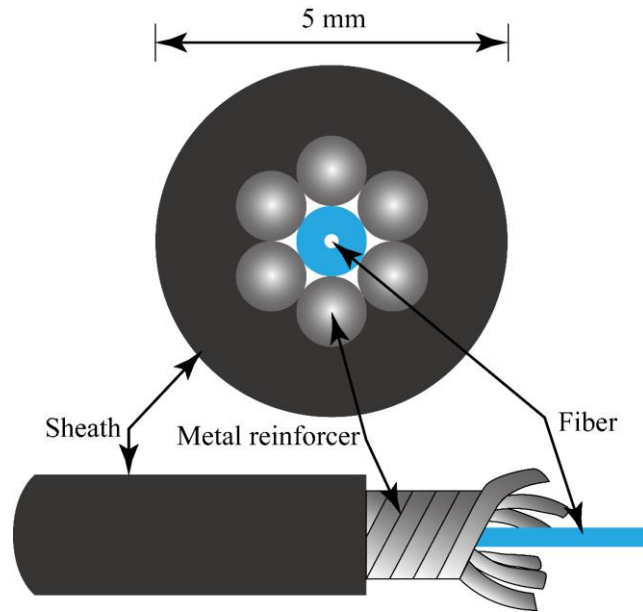
$$80 \quad v_B(\varepsilon) = v_B(0) + \frac{dv_B(\varepsilon)}{d\varepsilon} \varepsilon \quad (1)$$

81 where $v_B(\varepsilon)$ is the Brillouin frequency against strain ε , $v_B(0)$ is the Brillouin frequency shift
82 without stain, $dv_B(\varepsilon)/d\varepsilon$ is the strain coefficient, and the proportional coefficient of strain, at a
83 wavelength of 1.55 μm , is approximately 0.5 GHz/%.

84 Following such a term, the strain distributed along the sensing optical fiber can be measured.
85 Given the monitoring scenario of land subsidence, the deformation field along the sensing
86 optical cable caused by soil compression or rebound at depth h can be calculated in accordance
87 with the measured strain, which yields:

$$\Delta d = \int_{h_1}^{h_2} \varepsilon(h) dh \quad (2)$$

89 In this paper, a metal-reinforced single-core cable (MRC) was used to measure the
90 subsurface deformation, whose structure is shown in Fig. 1. The MRC, which can effectively
91 protect the optical fibers with several metal reinforcers, has good coupling and uniformity with
92 soil due to the screw structure of the sensor surface (Gu et al., 2018), the type of MRC in this
93 test is NZS-DSS-C02.



94
95 Fig. 1. The structure of a metal-reinforced single-core cable (MRC).

96 Note DFOS acquires mass strain measurements; to efficiently extract the morphological
97 distributions along with the underground depth, the measurements ought to be organized in the
98 form of a space-time matrix \mathbf{B} (Sun et al., 2014). Given that the total number of sampling points

99 along the optical fiber is n and the total number of sampling times is m , \mathbf{B} is a two-dimensional
 100 matrix with n rows and m columns, which yields:

$$101 \quad \mathbf{B} = \begin{bmatrix} \varepsilon_{00} & \varepsilon_{10} & \text{L} & \varepsilon_{j0} & \text{L} & \varepsilon_{m0} \\ \varepsilon_{01} & \varepsilon_{11} & \text{L} & \varepsilon_{j1} & \text{L} & \varepsilon_{m1} \\ \text{L} & \text{L} & \text{L} & \text{L} & \text{L} & \text{L} \\ \varepsilon_{0i} & \varepsilon_{1i} & \text{L} & \varepsilon_{ji} & \text{L} & \varepsilon_{mi} \\ \text{L} & \text{L} & \text{L} & \text{L} & \text{L} & \text{L} \\ \varepsilon_{0n} & \varepsilon_{1n} & \text{L} & \varepsilon_{jn} & \text{L} & \varepsilon_{mn} \end{bmatrix} \quad (3)$$

102 where the element ε_{ij} is the measurements of the strain field on the measuring point with
 103 different depth i at sampling time j .

104 Now that using the DFOS for subsidence monitoring, the submatrix \mathbf{B}_s of the space-time
 105 matrix \mathbf{B} is usually extracted to characterize the local distribution of stratum deformation field,
 106 which yields:

$$107 \quad \mathbf{B}_s = \begin{bmatrix} \varepsilon_{us} & \text{L} & \varepsilon_{js} & \text{L} & \varepsilon_{vs} \\ \text{L} & \text{L} & \text{L} & \text{L} & \text{L} \\ \varepsilon_{ui} & \text{L} & \varepsilon_{ji} & \text{L} & \varepsilon_{vi} \\ \text{L} & \text{L} & \text{L} & \text{L} & \text{L} \\ \varepsilon_{ut} & \text{L} & \varepsilon_{jt} & \text{L} & \varepsilon_{vt} \end{bmatrix} \quad (4)$$

108 where the time interval of sampling points of the submatrix \mathbf{B}_s is $[u, v]$, and that of the sampling
 109 depth interval is $[s, t]$. The submatrix \mathbf{B}_s can also be represented as a column vector group,
 110 which yields:

$$111 \quad \mathbf{B}_s = \begin{bmatrix} \mathbf{E}_u, \mathbf{E}_{u+1} \text{L} \mathbf{E}_j \text{L} \mathbf{E}_v \end{bmatrix} \quad (5)$$

112 where

$$113 \quad \mathbf{E}_j = \begin{bmatrix} \varepsilon_{js}, \varepsilon_{j,s+1} \text{L} \varepsilon_{jt} \end{bmatrix}^T \quad (6)$$

114 The column vector E_j represents the strain vector acquired by the DFOS at the depth range $[s,$
115 $t]$ at sampling time j . The column vector E_j at a certain time is substituted into Eq. (2) to obtain
116 the ground deformation Δd at a specific depth range $[s, t]$, which yields:

$$117 \quad D d_{st} = \int_{h_s}^{h_t} \varepsilon_{ji} dh_i \quad (7)$$

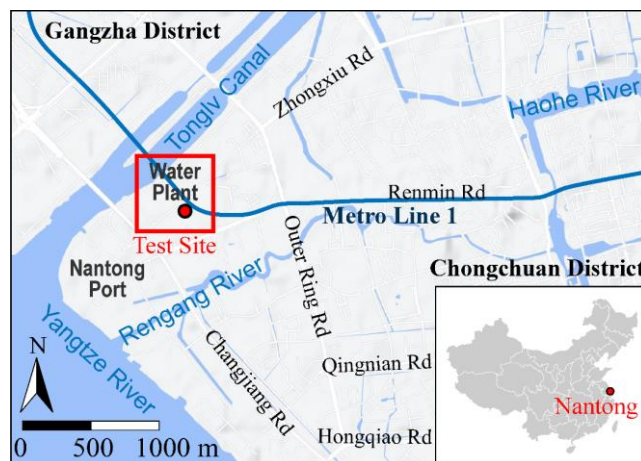
118 where h_i is the length of a certain measured micro-element section of the DFOS in the formation.

119 **3. Pumping test**

120 **3.1 Conditions of engineering geology and hydrogeology**

121 Nantong, a coastal city in eastern China, has planned to build four metro lines. Among those,
122 the planned section between the Jianghai Avenue Station and the Bus Station of Metro Line 1
123 will travel beneath the emergency water source of the Nantong Port Water Plant. The tunnel
124 has a circular section with a burial depth of 21 m. The lining structure has an inner diameter of
125 5.5 m and a thickness of 0.35 m. In accordance with the relevant specifications (Gao et al.,
126 2010), the cumulative settlement of the layer where the tunnel is located should not exceed 20
127 mm, and the curvature radius of the longitudinal deformation curve is not less than 15,000 m.
128 Given the emergency water supply, a large amount of groundwater will be extracted from the
129 aquifer. This may induce subsidence within the overlying strata, which might in turn pose some
130 threats to the operational safety of the metro. This paper characterizes the adverse impacts of
131 emergency pumping on the metro tunnel by monitoring the subsurface deformation field
132 induced by a test of multi-well dewatering.

133 Nantong is located in the alluvial plain of the Yangtze River Delta, widely covered by the
134 Quaternary strata. The thickness of the strata ranges from 200 to 360 m, which is composed of
135 a set of multiple sedimentary cycles with alternating sand and clay layers. The pumping test
136 was performed on the south bank of the estuary of the Tonglv Canal into the Yangtze River, as
137 shown in Fig. 2. The geographic location of the testing site is $32^{\circ}00'55''\sim 32^{\circ}01'16''$ North
138 latitude and $120^{\circ}49'11''\sim 120^{\circ}49'33''$ East longitude, with a site altitude of about 4.0 m. Nantong
139 has a humid subtropical monsoon climate with an annual average temperature of 16°C ,
140 precipitation of 1036 mm, and evaporation of 1392 mm.



141

142

Fig. 2. Location of the test site.

143 Table 1 lists the physical and mechanical parameters of the strata of the test site according
144 to the preliminary investigation works. As seen from the table, the strata are mainly composed
145 of sandy soils mixed with silty clayey soils. Among those, the silt layer at a depth of 50 m
146 attains a great amount of water content, as well as a small compression modulus. The
147 permeability varies between the silty clay and silty sand interlayers within both ranges of 120
148 to 150 m and 180 to 190 m. Note both interlayers might impede the transit of groundwater,

149 which causes the inconsistency between the deformation fields of the subsurface and the ground
 150 surface.

151 Table 1. Physical and mechanical parameters of soils.

Soil layer	Depth (m)	w (%)	G_s	ρ (kN/m ³)	E_s (MPa)	c (kPa)	φ (°)
Filling	5	28.2	2.7	18.2	9.1	14.1	17.6
Silty sand	30.3	22.5	2.7	19.6	13.9	6.4	26.8
Silty clay	49.5	32.7	2.2	15.7	7.8	15.4	19.8
Medium sand	116.5	18.3	2.7	19.6	16.4	2.4	32.7
Silty clay	133.0	23.8	2.7	20.0	10.9	43.6	20.6
Fine sand	146.5	20.7	2.7	19.4	13.5	3.0	32.2
Clay	181.0	22.6	2.7	19.8	11.4	110.4	22.7
Fine sand	187.9	21.8	2.3	17.3	21.3	16.9	31.7
Silty clay	193.2	24.8	2.3	17.0	14.2	3.3	31.2
Medium sand	225.5	19.8	2.7	19.0	11.8	3.4	31.5
Clay	230.0	20.7	2.8	20.8	14.4	116.1	20.3

152 The groundwater is mainly pore water, mostly stored in sand layers. In accordance with the
 153 storage condition, the groundwater can be divided into five aquifer groups from top to bottom,
 154 namely, the phreatic aquifer (PA), the 1st confined aquifer (CA1), the 2nd confined aquifer
 155 (CA2), the 3rd confined aquifer (CA3) and the 4th confined aquifer (CA4). Note that only CA4
 156 is not included in this test.

157 The PA consists of the silty clay, silty sand, and fine sand of the Yangtze Delta phase of
 158 Holocene (Q_h), buried upon a shallow depth of 50 m. The depth of the water level, seasonally
 159 varying from 1 to 3 m, is affected by the atmospheric precipitation and surface runoff. The layer
 160 of PA is characterized by the coarse particles in the upper and lower sections and fine particles
 161 in the middle section along the vertical direction; some sections of the lower aquifer are

162 connected to CA1. The dewatering amount of a single-well is about 10~20 m³/d, with poor
163 water quality and thus few exploitations.

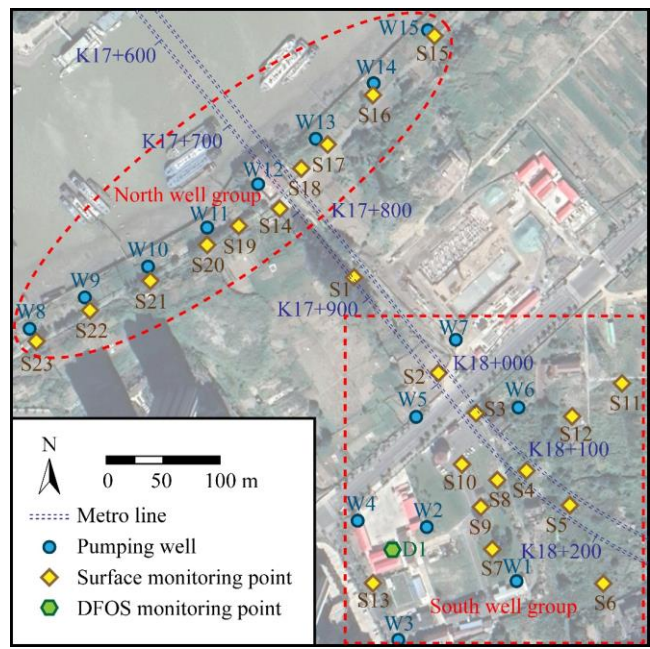
164 The CA1 consists of alluvial and marine loose sands of the Upper Pleistocene (Q_{p3}), with a
165 burial depth ranging from 50 to 110 m. The lithology of the aquifer mainly consists of pebbles,
166 gravel, coarse sand, medium sand, fine sand, and silty sand; those soil particles, from coarse to
167 fine, are vertically distributed from bottom to top. The aquifer has high permeability and thus
168 enough groundwater supply, which is closely connected to the upper aquifer PA and lower
169 aquifer CA2. The dewatering amount of a single-well is about 2000~3000 m³/d, also with poor
170 water quality.

171 The CA2 consists of the fine sand and silty sand layers of the fluvial and estuarine
172 sedimentary of Middle Pleistocene (Q_{p2}), buried from 130 to 150 m. Note the water barrier
173 between CA1 and CA2 is partially missing. The dewatering amount of a single-well is about
174 300~3000 m³/d, still with poor water quality.

175 Aquifer CA3 consists of gravelly medium sand, fine sand, and locally gravelly cobble of
176 river-lake sedimentary of the Lower Pleistocene (Q_{p1}), whose buried depth ranges from 180 to
177 240 m, with an uneven thickness ranging from 20 to 100 m. The dewatering amount of a single-
178 well is generally over 2000 m³/d. Both the quality and quantity of the groundwater are good
179 and rich, which makes CA3 the main exploited freshwater aquifer of Nantong city. Note that
180 in this test, the groundwater is extracted from aquifer CA3, with a well depth of 225 m.

181 **3.2 Test layout and schedule**

182 Fifteen pumping wells, labeled from W1 to W15, of the Nantong Port Water Plant near the
183 metro line 1 were selected for this test. All wells were pumped at a rate of 80 t/h under the
184 emergency water supply conditions, from August 9 to 15, 2018. The layout of the pumping
185 wells and monitoring points is shown in Fig. 3. Two well groups exist in the test site, namely
186 the south well group, W1 to W7, located near the water plant on the southern side, and the north
187 well group, W8 to W15, at the river bank on the northern side. In addition, 23 monitoring points
188 of ground surface settlement, labeled as S1 to S23, were deployed near the metro line and both
189 pumping well groups.



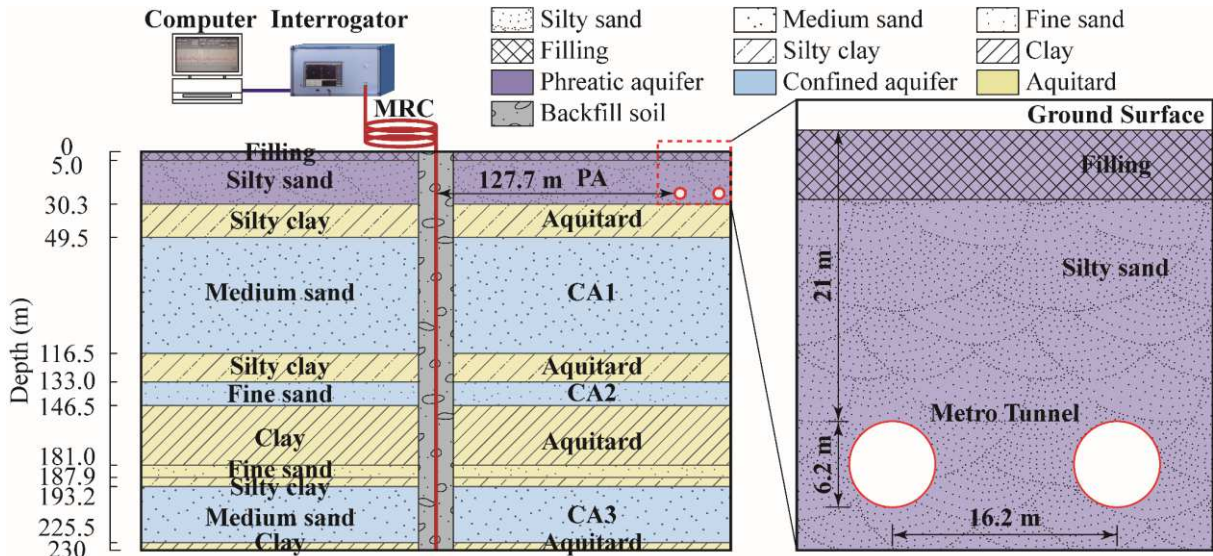
190

191

Fig. 3. Test layout.

192 Given the subsurface deformation field might vary from that of the surface ground, a
193 borehole (D1), with a depth of 230 m and a diameter of 129 mm, was deliberately drilled and
194 a metal-reinforced single-core cable (MRC) was laid inside to measure the vertical subsurface

195 deformation field. Fig. 4 illustrates the measuring layout of the DFOS monitoring system. The
 196 end of the MRC was connected to a BOTDR interrogator, which can process and record the
 197 strain field data along with the optical cable. The parameters of the interrogator are listed in
 198 Table 2. Before the pumping, the borehole was backfilled with special fillings to make the
 199 MRC fully couple with the surrounding soils. To synchronize the deformation of fiber with the
 200 subsurface strata, fine sand-clay soft aggregate, similar to the site strata, was used for the
 201 backfill material in the borehole. The deformation modulus of the backfill soil was adjusted
 202 with different ratios of fine sand and clay, and the backfill soil with the same deformation
 203 modulus to the surrounding strata at different depths in the borehole (Zhang et al., 2020). The
 204 instrument was calibrated at the site after the cable having been fully coupled with the strata.



205
206 Fig. 4. The layout of subsurface deformation monitoring.

207 Table 2. Parameters of the BOTDR interrogator.

Model	Resolution	Accuracy	Range	Distance	Operating wavelength	Scanning interval
AV6419	0.05 m	$\pm 10 \mu\epsilon$	$\pm 15000 \mu\epsilon$	0.5 km	1550 \pm 5 nm	5 MHz

208

209 Three monitoring items, including water level, surface settlement, and subsurface
 210 deformation field, were performed during the test. The monitoring of the water level of the
 211 wells was implemented until no obvious variation can be observed. Three leveling calibrations
 212 were conducted before pumping on June 11, June 28, and July 17, 2018, respectively.
 213 Meanwhile, three rounds of DFOS measurements were acquired for calibration on Nov. 21,
 214 Dec. 25, 2017, and Jan. 16, 2018, respectively. The monitoring schedule is depicted in Table 3.
 215 Note that three rounds of DFOS measurements were collected per occurrence date.

216 Table 3. Occurrence dates of measurement.

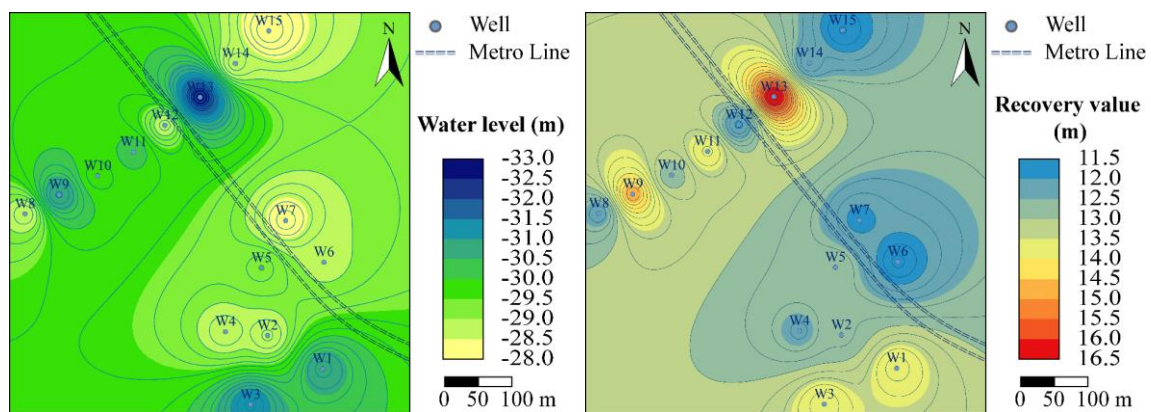
Period	Leveling	DFOS
Pumping	Aug. 10; Aug. 13; Aug. 15	Aug. 9~15
Postpumping	Aug. 18; Aug. 24; Aug. 30; Sep. 11; Sep. 28;	Aug. 16; Aug. 30; Sep. 5; Sep. 22;
	Oct. 15; Oct. 26; Nov. 17; Nov. 29; Dec. 11; Dec. 23, 2018; Jan. 4; Jan. 16, 2019	Oct. 10; Oct. 25; Nov. 13; Dec. 27, 2018; Jan. 20, 2019

217 4. Measuring results

218 4.1 Water level variation

219 From Aug. 9 to 15, 2018, the group pumping was conducted synchronously on the 15 wells
 220 in Fig. 3. After stopping pumping for 30 days, the water level tended to be stable. The
 221 measurements exhibit that before pumping, the initial water levels of the 15 wells were almost
 222 the same, approximately -16.1~-17.5 m. The water level sharply dropped during the pumping;
 223 the decline rate of water level gradually slowed. The water level attained its minimum on the
 224 sixth day of pumping. Fig. 5 (a) shows the distribution of the water level. As noted from the
 225 figure, a total level drop of 11.39~16.50 m occurred on Aug. 15. Subsequently, a sharp rebound
 226 of water level occurred on Aug. 16 right after the pumping; while the rebound rate obviously

227 slowed down from Aug. 22. On August 30, 15 days after the pumping, the water level was
 228 almost restored to its initial value, only with a level falling of 0.05~0.65 m. The distribution of
 229 the recovery values of water level is shown in Fig. 5(b). As seen from Fig. 5, the greatest decline
 230 of the water level occurred near the center of the northern wells (W13), which is located near
 231 both the river bank and the metro line. Note the rise and drop of water level exhibit similar
 232 distribution patterns, suggesting the soil permeability of the west side is greater than that of the
 233 east side, and the groundwater on the east side attains a stronger rechargeability.



234
235 Fig. 5. Water level variation.

236 (a) Distribution of water level on Aug. 15;

237 (b) Distribution of water level recovery on Aug. 30.

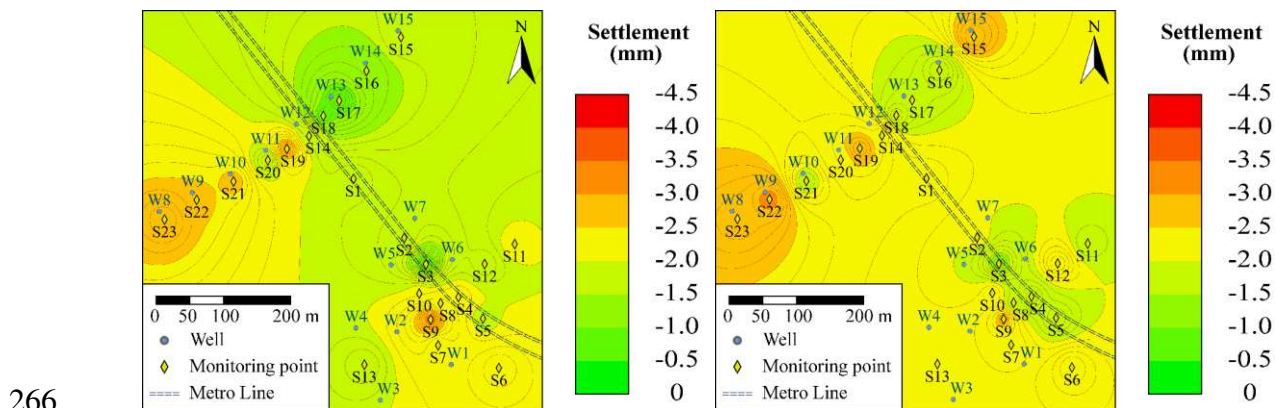
238 **4.2. Surface settlement**

239 Fig. 6 shows the distribution patterns of the ground surface settlement, in which Fig. 6 (a)
 240 and (b) exhibit those during the pumping. As seen from Fig. 6 (a), at the initial stage of pumping,
 241 a large settlement occurred on the west side of the north well group; and also, a small range of
 242 settlement occurred in the south well group. The greatest settlement occurred at the measuring
 243 point S9, with a settlement value of 2.9 mm. Tiny settlement occurred on the rest part. As seen

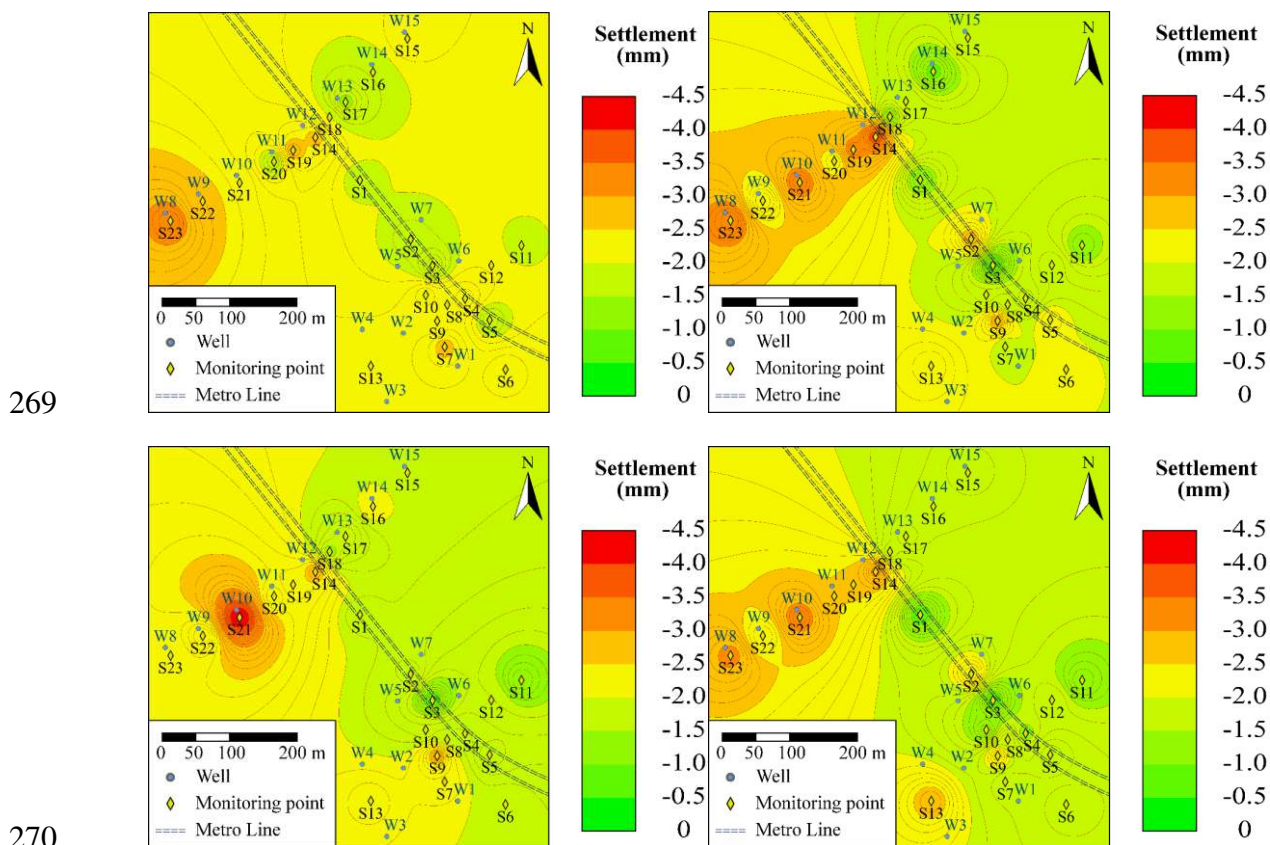
244 from Fig. 6 (b), with the continuous pumping, a small amount of settlement appears on the wide
245 range of the site, and the settlement area of the west side of the north well group enlarged a
246 little. The maximum of settlement occurred on measuring point S22, with a settlement value of
247 3.1 mm. In addition, the settlement values of the east side of the embankment and the south
248 well group are both small, suggesting a plenty supply of groundwater.

249 Fig. (7) shows the distribution pattern of settlement within the five months after the pumping.
250 As shown from Fig. 7(a), within two weeks after the end of pumping, the settlement range
251 further enlarged, and the maximum settlement, with a value of 3.3 mm, occurred on measuring
252 point S23, the west side near the embankment, suggesting that the settlement behavior lagged
253 the deep pumping activity. As seen from Fig. 7 (b), the settlement area gradually merged to
254 exhibit a large range of the settlement area, which is similar to the distribution pattern of the
255 variation of water levels in the wells. A large settlement occurred on the west side of the north
256 well group and the distribution is continuous. The maximum of the settlement occurred at the
257 measuring point S14, with a settlement value of 3.8 mm. As seen from Fig. 7 (c), the settlement
258 area did not vary significantly 3 months after the pumping. However, a notably concentrated
259 settlement occurred on measuring point S21, on the west side of the embankment, with a value
260 of 4.4 mm, which is the greatest settlement value of the test, again manifesting that the ground
261 settlement lags the deep pumping. As seen from Fig. 7 (d), the settlement at the measuring point
262 S21 gradually dissipated and its range expanded. The settlement value decreased to 3.3 mm.
263 Note that no obvious ground settlement occurred in this test, suggesting that the existence of

264 multiple aquitards impeded the free transfer between different aquifers. Also, the test results
 265 indicate that the permeability of the strata on the west side is greater than that of the east side.



267 Fig. 6. The variation of surface settlement distribution during the pumping.
 268 (a) Aug. 10, 2018; (b) Aug. 15, 2018.



271 Fig. 7. The variation of surface settlement distribution after the pumping.
 272 (a) Aug 24, 2018; (b) Sep. 11, 2018; (c) Nov. 17, 2018; (d) Jan. 16, 2019.

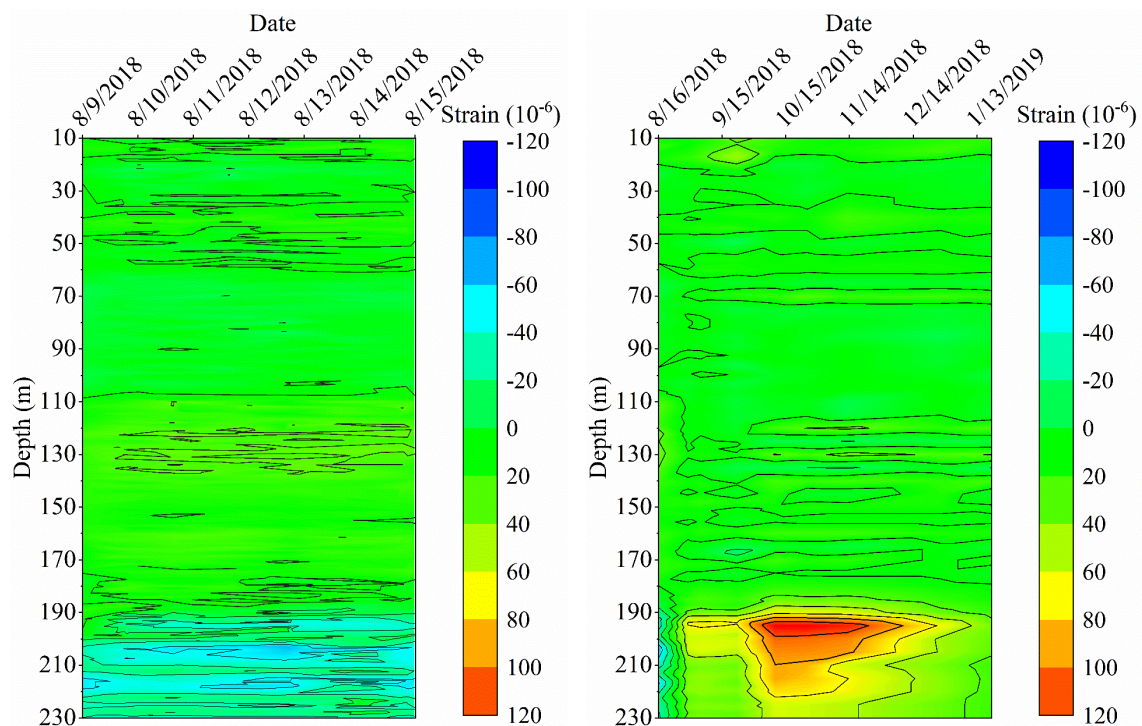
273 **4.3. Characterization of the subsurface deformation field**

274 In order to further study the influence of the groundwater barrier on the deformation
275 connectivity of the strata, the subsurface deformation values acquired by DFOS were
276 substituted into the space-time matrix B . Note the buried depth of the constant-temperature
277 layer of the test site is from 10 to 230 m; thus, the measurements of the strain field ranging
278 from the ground surface to 10 m underground were excluded owing to the measuring
279 uncertainty induced by the temperature variation in the variable temperature layer. Thus, the
280 submatrices of the constant-temperature layer were extracted to plot the strain field contours
281 during and after the pumping, as shown in Fig. 8. As can be noted from the figure, the strain
282 concentrates within the acquire layers in Fig. 4. Specifically, restricted by the aquiclude of the
283 clayey layer ranging from the buried depth of 150 to 180 m, the greater strain mainly occurs
284 within aquifer CA3 from the buried depth of 180~230 m.

285 As seen from Fig. 8(a), during the pumping, the strain values within the buried depth of
286 10~180 m were tiny. Note obvious compressive strain occurred within aquifer CA3, which
287 corresponds to average daily subsidence of approximately 1.61~2.87 mm calculated by Eq. (7).

288 As seen from Fig. 8(b), after the pumping, the strata strain field, ranging from the buried
289 depth of 10~180 m, varied slightly; while the significant variation of the strata strain field
290 occurred within 180~230 m underground. Although the strata exhibited compressive strain at
291 the immediate end of pumping, tensile strain started occurring in half a month, suggesting the
292 existence of an obvious and rapid stratum rebound and the rebound evolved from top to bottom.
293 One month after the end of pumping, the rebound extended from the upper part to the entire

294 aquifer CA3. Four months after the end of pumping, the rebound rate slowed down owing to
295 the gradual recharging of the groundwater. The stratum rebound of aquifer CA3 ranges from
296 1.89~2.15mm, calculated by Eq. (7).



297

298

Fig. 8. Contour plot of the subsurface strain field.

299

(a) During the pumping; (b) After the pumping.

300

The stratigraphic strain field is converted to the accumulated subsurface deformation in

301

accordance with Eq. (7). Fig (9) compares variation trends of both cumulative subsurface

302

deformation of aquifer CA3 and the corresponding surface settlement over time. As seen from

303

the figure, the surface subsided slightly during the pumping. After the pumping, the settlement

304

rate slowed down, and the maximum of settlement is 3.2 mm, occurring on the 44th day, and

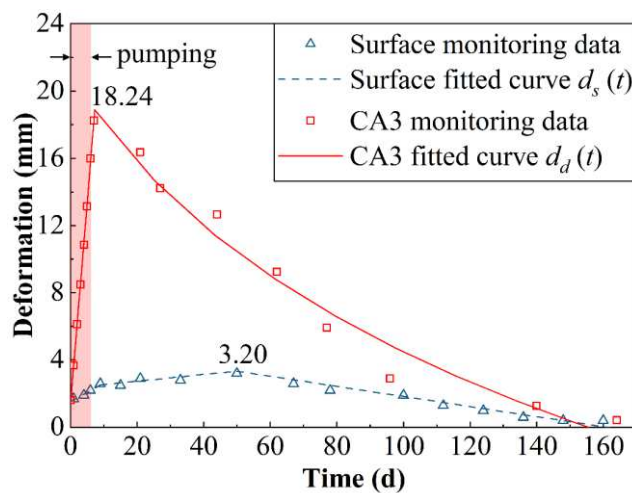
305

then rebounded with small fluctuation. Meanwhile, a sharp compressive deformation of aquifer

306

CA3 occurred during the pumping, and the deformation varied linearly with time. The

307 deformation value reached the maximum of 18.24 mm on the first day after the end of the
 308 pumping, and then a rebound occurred, whose rate slowed down with time. The deformation
 309 of CA3 returned to the initial state five months after the end of pumping. Compared with the
 310 subsurface deformation of CA3, the surface settlement is smaller and lagged about 1 to 2
 311 months, suggesting the subsidence induced by the deep pumping is gradually transmitted to the
 312 surface.



313
 314 Fig. 9. Ground deformation trends and fitted curves of borehole D1.

315 **5. Discussion**

316 **5.1 Analysis of cumulative ground settlement**

317 As seen from Fig. 9, during the pumping state, aquifer CA3 and surface settlement increased
 318 linearly over time; during the postpumping stage, the surface settlement continued to increase
 319 linearly, but the rate decreased, while aquifer CA3 exhibited a nonlinear rebound trend. Note
 320 linear functions are used to fit aquifer CA3 and surface settlement trend during the pumping.
 321 The logarithmic function is used to fit the rebound trend of CA3 during the postpumping, and

322 a piecewise linear function is used to fit the surface subsidence and the rebound trend of the
 323 postpumping stage, respectively. Eqs. (8) and (9) are the fitting functions of the deformation
 324 trends of CA3 and ground surface, respectively.

$$325 \quad d_d(t) = \begin{cases} 1.37+2.40t & t \leq 7 \\ 72.39-13.69\ln(t+42.57) & t > 7 \end{cases} \quad (8)$$

326 where $d_d(t)$ (in mm) is the cumulative deformation of aquifer CA3, and t (in days) is the duration.

327 Eq. (8) suggests that continuous pumping within the aquifer would induce sharp subsurface
 328 deformation. The underground rebound follows a logarithmic trend and the rebound rate
 329 slowed down with time.

$$330 \quad d_s(t) = \begin{cases} 1.53+0.11t & t \leq 9 \\ 2.34+0.02t & 9 < t \leq 50 \\ 4.84-0.03t & t > 50 \end{cases} \quad (9)$$

331 where $d_s(t)$ (in mm) is the cumulative settlement of surface, and t (in days) is the duration.

332 Eq. (9) shows that the surface will undergo linear settlement over time during the pumping,
 333 and will continue to settle at a low rate after the pumping. This stage of settlement lasted as
 334 long as 43 days; such comprises the major part of the total settlement. Subsequently, the surface
 335 rebounded linearly with time, and the time recovering to the initial state was the same as that
 336 of CA3, suggesting the surface settlement after the pumping is closely related to the subsurface
 337 deformation.

338 Note that the surface settlement was divided into two phases, the former was closely
 339 associated with the pumping and the latter was closely related to CA3 stratigraphic deformation.
 340 The duration of the surface settlement was nearly 50 days, which is about 1/3 of the time
 341 required for the surface rebound, and the time required for both aquifer CA3 and surface to

342 recover to their initial state was about 150 days. When the water source pumping continuously
 343 for t_p days ($t_p > 6$), the duration of the formation to recover to its initial state is t_t , then according
 344 to Eq. (8) satisfies

$$345 \quad 72.39 - 13.69 \ln \left[(t_t - t_p + 6) + 42.57 \right] + 2.4(t_p - 6) = 0 \quad (t_p > 6) \quad (10)$$

346 Eq. (10) is derived to obtain the total recover duration of the strata t_t and the duration of ground
 347 surface settlement t_s , namely,

$$348 \quad t_t = 3t_s = \exp \left(\frac{57.99 + 2.4t_p}{13.69} \right) - 48.57 + t_p \quad (t_p > 6) \quad (11)$$

349 Substituting into Eq. (9), the maximum surface settlement is

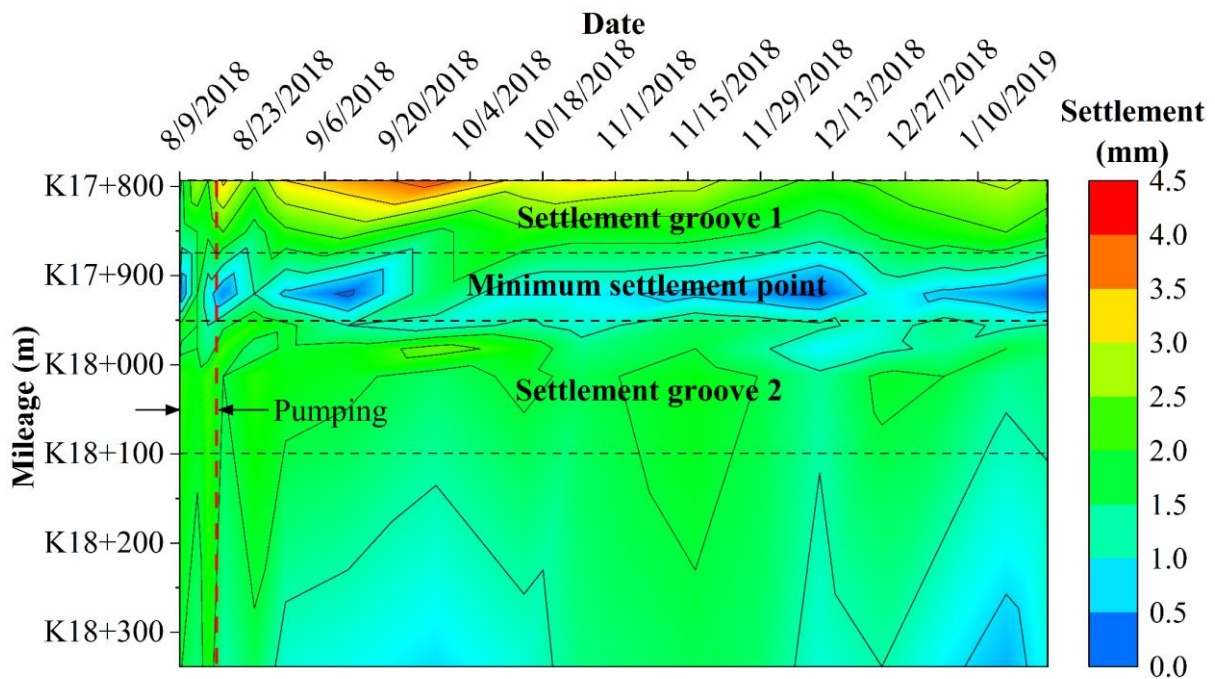
$$350 \quad \begin{aligned} d_s(t_p) &= 2.34 + 0.02 \times t_s \\ &= 2.02 + 0.02t_p + 1.38 \exp(0.175t_p) \quad (t_p > 6) \end{aligned} \quad (12)$$

351 According to Eq. (12), the maximum surface settlement increases approximately
 352 exponentially with the duration of the pumping. Once the dewatering lasts for more than 15
 353 days, the ground settlement will reach 21.4 mm, exceeding the safety limit of 20 mm given by
 354 the relevant specifications (Gao et al., 2010). Therefore, the limit duration of continuous
 355 dewatering should not exceed 15 days.

356 **5.2 Analysis of the curvature radius along the metro line**

357 Metro tunnel, as a typical linear distribution structure, is more sensitive to uneven
 358 deformation of the ground along the line. From Fig. 6 and Fig. 7, the settlement differences in
 359 the site traversed by this metro were more significant than those in other areas. The settlement
 360 data from the settlement monitoring points along the metro line (S14, S1, S2, S3, S4, S5, and
 361 S6) were selected to draw the trend plot of cumulative surface settlement along the metro line

362 with time by the linear interpolation method, as shown in Fig. 10. The settlement was much
 363 less than the specification limit of 20 mm (Gao et al., 2010). Also, obvious settlement grooves
 364 occurred in both well groups, respectively, in the middle of which the settlement amount attains
 365 the minimum. Note excessive relative settlement reduced the subsidence curvature radius.

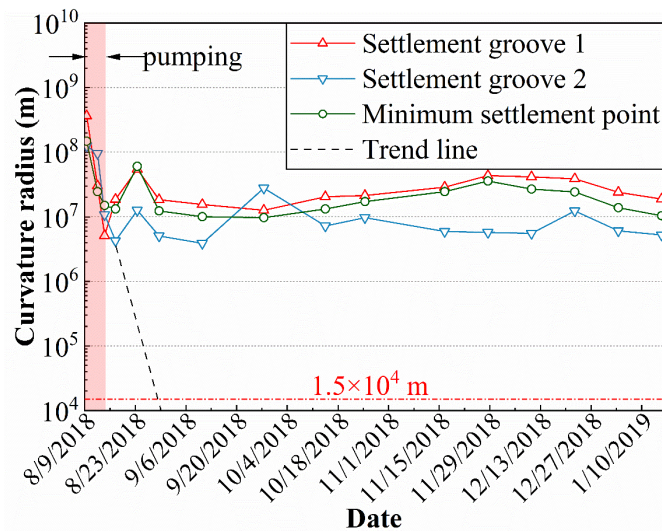


366

367 Fig. 10. Settlement distribution along the metro line.

368 The curvature radius, at each monitoring point along the metro line, induced by the
 369 longitudinal deformation of the tunnel was calculated by the three-point method (Cupec et al.,
 370 2009). Statistically, a relatively small curvature radius occurred on three points, including both
 371 settlement grooves and their middle point. The variation trends of the curvature at those three
 372 points were plotted in Fig. 11. As seen from the figure, the minimum curvature radius along
 373 the metro line occurred at settlement groove 2 on September 11, with a radius of 3.89×10^6 m.
 374 Note that is much greater than the 1.5×10^4 m specified by the specification, indicating that the
 375 short-term dewatering activity has less influence on the tunnel. Also, note that the curvature

376 radius of those key points decreases exponentially with time during the pumping. Once the
 377 pumping last more than 15 days, the curvature radius will be less than the standard value.
 378 Within the first week after the end of the pumping, the curvature radius rose rapidly and then
 379 fluctuated steadily, suggesting the variation of the longitudinal curvature radius of the tunnel is
 380 closely related to the dewatering activities along the metro line.



381
 382 Fig. 11. The minimum curvature radius of typical sections along the metro line.

383 **6. CONCLUSIONS**

384 (1) The maximum surface settlement, produced by the 6-day pumping test, was about 4.4
 385 mm, which is less than the 20 mm limit required by the metro protection; the minimum
 386 curvature radius was 3.89×10^6 m, which is much greater than the minimum limit of 1.5×10^4 m
 387 for the longitudinal deformation safety as specified in the specification.

388 (2) The fiber optic cable, vertically buried in the constant-temperature layer, can effectively
 389 measure the subsurface strain field and be used to deduce the deformation amount of each
 390 stratum based on the measurements.

391 (3) After the end of pumping, a large settlement occurred on the west side of the test site,
392 which is consistent with the distribution pattern of groundwater level, suggesting the overall
393 distribution of settlement is combinedly affected by the formation permeability and
394 groundwater rechargeability.

395 (4) Influenced by the vertical distribution of aquitards, deep pumping causes the deformation
396 of the aquifers to be much greater than the surface settlement. Note the surface settlement lags
397 behind the settlement of the aquifer by 1 to 2 months; the surface rebound recovery also exhibits
398 a similar delay.

399 (5) During the pumping, the deformation of the aquifer and ground surface is linearly
400 compressed with time. After the pumping, the ground surface continues to settle linearly at a
401 slower rate for about 50 days, followed by a slow linear rebound; the aquifer is logarithmically
402 rebounded. Both rebounded to the initial state in about 150 days.

403 (6) During the pumping, the curvature radius of the settlement grooves along the metro line
404 decreased exponentially with time, and started to rise rapidly and maintained steady
405 fluctuations one week after the end of the pumping.

406 (7) Although the short-term continuous water supply from the groundwater source has
407 negligible adverse effects on the metro tunnel, the stratigraphic deformation fitting equations
408 indicates that the source should not be continuously pumped for more than 15 days.

409 **ACKNOWLEDGMENTS**

410 The authors would like to thank the anonymous reviewers for their helpful comments and
411 suggestions. This study was financially supported by the China Geological Survey (CGS)
412 Yangtze River Delta Area Nanjing-Shanghai-Wenzhou Urban Planning Area 1:50,000
413 Environmental Geological Survey Project (DD20160246) and the National Science Foundation
414 of China (grant Nos. 42077232).

415 **REFERENCES**

- 416 Abidin HZ, Djaja R, Darmawan D, Hadi S, Akbar A, Rajiyowiryo H, Sudibyo Y, Meilano I, Kasuma MA,
417 Kahar J, Subarya C (2001) Land subsidence of Jakarta (Indonesia) and its geodetic monitoring system.
418 *Natural Hazards* 23:365-387.
- 419 Baldi P, Casula G, Cenni N, Loddo F, Pesci A (2009) GPS-based monitoring of land subsidence in the Po Plain
420 (Northern Italy). *Earth and Planetary Science Letters* 288:204-212.
- 421 Budhu M, Adiyaman IB (2010) Mechanics of land subsidence due to groundwater pumping. *International*
422 *Journal for Numerical and Analytical Methods in Geomechanics* 34:1459-1478.
- 423 Calderhead AI, Therrien R, Rivera A, Martel R, Garfias J (2011) Simulating pumping-induced regional land
424 subsidence with the use of InSAR and field data in the Toluca Valley, Mexico. *Advances in Water*
425 *Resources* 34:83-97.
- 426 Chai J, Shen S, Zhu H, Zhang X (2004) Land subsidence due to groundwater drawdown in Shanghai.
427 *Geotechnique* 54:143-147.
- 428 Choudhury P, Gahalaut K, Dumka R, Gahalaut VK, Singh AK, Kumar S (2018) GPS measurement of land
429 subsidence in Gandhinagar, Gujarat (Western India), due to groundwater depletion. *Environmental Earth*
430 *Sciences* 77:770. doi:10.1007/s12665-018-7966-5
- 431 Cui Z, Jia Y (2018) Physical model test of layered soil subsidence considering dual effects of building load and
432 groundwater withdrawal. *Arabian Journal for Science and Engineering* 43:1721-1734.
- 433 Cupec R, Grbić R, Sabo K, Scitovski R (2009) Three points method for searching the best least absolute
434 deviations plane. *Applied Mathematics and Computation* 215:983-994.
- 435 Edalat A, Khodaparast M, Rajabi AM (2020) Scenarios to control land subsidence using numerical modeling of
436 groundwater exploitation: Aliabad plain (in Iran) as a case study. *Environmental Earth Sciences* 79:494.
437 doi:10.1007/s12665-020-09246-2
- 438 Galloway DL, Burbey TJ (2011) Review: Regional land subsidence accompanying groundwater extraction.
439 *Hydrogeology Journal* 19:1459-1486.

440 Gao G, Gao M, Yang C, Yu Z (2010) Influence of deep excavation on deformation of operating metro tunnels
441 and countermeasures. *Chinese Journal of Geotechnical Engineering* 32:453-459.

442 Gu K, Shi B, Liu C, Jiang H, Li T, Wu J (2018) Investigation of land subsidence with the combination of
443 distributed fiber optic sensing techniques and microstructure analysis of soils. *Engineering Geology* 240:34-
444 47.

445 Herrera-García G, Ezquerro P, Tomás R, Béjar-Pizarro M, López-Vinielles J, Rossi M, Mateos RM, Carreón-
446 Freyre D, Lambert J, Teatini P, Cabral-Cano E, Erkens G, Galloway D, Hung W-C, Kakar N, Sneed M,
447 Tosi L, Wang H, Ye S (2021) Mapping the global threat of land subsidence. *Science* 371:34-36.
448 doi:10.1126/science.abb8549

449 Hu J, Chu H, Hou C, Lai T, Chen R, Nien P (2006) The contribution to tectonic subsidence by groundwater
450 abstraction in the Pingtung area, southwestern Taiwan as determined by GPS measurements. *Quaternary*
451 *International* 147:62-69.

452 Jiang X, Gao Y, Wu Y, Lei M (2016) Use of Brillouin optical time domain reflectometry to monitor soil-cave
453 and sinkhole formation. *Environmental Earth Sciences* 75:225. doi:10.1007/s12665-015-5084-1

454 Kearns TJ, Wang G, Bao Y, Jiang J, Lee D (2015) Current land subsidence and groundwater level changes in the
455 houston metropolitan area (2005-2012). *Journal of Surveying Engineering* 141.

456 Motagh M, Shamshiri R, Haghighi MH, Wetzel H-U, Akbari B, Nahavandchi H, Roessner S, Arabi S (2017)
457 Quantifying groundwater exploitation induced subsidence in the Rafsanjan plain, southeastern Iran, using
458 InSAR time-series and in situ measurements. *Engineering Geology* 218:134-151.

459 Mousavi SM, Shamsai A, Naggar MHE, Khamehchian M (2001) A GPS-based monitoring program of land
460 subsidence due to groundwater withdrawal in Iran. *Canadian Journal of Civil Engineering* 28:452-464.

461 Othman A, Abotalib AZ (2019) Land subsidence triggered by groundwater withdrawal under hyper-arid
462 conditions: case study from Central Saudi Arabia. *Environmental Earth Sciences* 78:243.
463 doi:10.1007/s12665-019-8254-8

464 Pacheco-Martínez J, Hernandez-Marín M, Burbey TJ, González-Cervantes N, Ortiz-Lozano JÁ, Zermeño-De-
465 Leon ME, Solís-Pinto A (2013) Land subsidence and ground failure associated to groundwater exploitation
466 in the Aguascalientes Valley, México. *Engineering Geology* 163:172-186.

467 Peng J, Huang Q, Hu Z, Wang M, Li T, Men Y, Fan W (2017) A proposed solution to the ground fissure
468 encountered in urban metro construction in Xi'an, China. *Tunnelling and Underground Space Technology*
469 61:12-25.

470 Poland M, Bürgmann R, Dzurisin D, Lisowski M, Masterlark T, Owen S, Fink J (2006) Constraints on the
471 mechanism of long-term, steady subsidence at Medicine Lake volcano, northern California, from GPS,
472 leveling, and InSAR. *Journal of Volcanology and Geothermal Research* 150:55-78.

473 Saleh M, Becker M (2018) New estimation of Nile Delta subsidence rates from InSAR and GPS analysis.
474 *Environmental Earth Sciences* 78:6. doi:10.1007/s12665-018-8001-6

475 Shen S, Wu H, Cui Y, Yin Z (2014) Long-term subsidence behaviour of metro tunnels in the soft deposits of
476 Shanghai. *Tunnelling and Underground Space Technology* 40:309-323.

477 Shen S, Xu Y (2011) Numerical evaluation of land subsidence induced by groundwater pumping in Shanghai.
478 *Canadian Geotechnical Journal* 48:1378-1392.

479 Sun Y, Zhang D, Shi B, Tong H, Wei G, Wang X (2014) Distributed acquisition, characterization and process
480 analysis of multi-field information in slopes. *Engineering Geology* 182:49-62.

481 Wang Y, Zhang M, Hu F, Dong Y, Yu K (2018) A coupled one-dimensional numerical simulation of the land
482 subsidence process in a multilayer aquifer system due to hydraulic head variation in the pumped layer.
483 *Geofluids* 2018.

484 Wang Z, Shen S, Cheng W, Xu Y (2016) Ground fissures in Xi'an and measures to prevent damage to the Metro
485 tunnel system due to geohazards. *Environmental Earth Sciences* 75:511.

486 Wu J, Jiang H, Su J, Shi B, Jiang Y, Gu K (2015) Application of distributed fiber optic sensing technique in land
487 subsidence monitoring. *Journal of Civil Structural Health Monitoring* 5:587-597.

488 Xu B, Yan C, Sun Q, Liu Y, Hou J, Liu S, Che C (2016a) Field pumping experiments and numerical simulations
489 of shield tunnel dewatering under the Yangtze River. *Environmental Earth Sciences* 75:715.
490 doi:10.1007/s12665-016-5493-9

491 Xu Y, Ma L, Du Y, Shen S (2012) Analysis of urbanisation-induced land subsidence in Shanghai. *Natural*
492 *Hazards* 63:1255-1267.

493 Xu Y, Shen S, Ren D, Wu H (2016b) Analysis of factors in land subsidence in shanghai: A view based on a
494 strategic environmental assessment. *Sustainability* 8:573.

495 Xue Y, Zhang Y, Ye S, Wu J, Li Q (2005) Land subsidence in China. *Environmental Geology* 48:713-720.

496 Zhang C, Shi B, Gu K, Liu S, Wu J, Zhang S, Zhang L, Jiang H, Wei G (2018) Vertically distributed sensing of
497 deformation using fiber optic sensing. *Geophysical Research Letters* 45:11732-11741.

498 Zhang C, Shi B, Zhu H, Wang B, Wei G (2020) Toward Distributed Fiber - Optic Sensing of Subsurface
499 Deformation: A Theoretical Quantification of Ground - Borehole - Cable Interaction. *Journal of*
500 *Geophysical Research: Solid Earth* 125.

501 Zhang C, Zhu H, Shi B, She J (2014) Interfacial characterization of soil-embedded optical fiber for ground
502 deformation measurement. *Smart Materials and Structures* 23:095022.

503 Zhang Y, Wu J, Xue Y, Wang Z (2017) Fully coupled three-dimensional nonlinear numerical simulation of
504 pumping-induced land movement. *Environmental Earth Sciences* 76:552.

505 Zheng G, Zeng C, Xue X (2014) Settlement mechanism of soils induced by local pressure-relief of confined
506 aquifer and parameter analysis. *Chinese Journal of Geotechnical Engineering* 36:802-817.

507 Zhou F, Xu J, Wang X (2017) Finite layer formulations for land subsidence due to groundwater withdrawal.
508 *International Journal of Geomechanics* 17.
509

Table headings

Table 1. Physical and mechanical parameters of soils.

Table 2. Parameters of the BOTDR interrogator.

Table 3. Occurrence dates of measurement.

Figure captions

Fig. 1. The structure of a metal-reinforced single-core cable (MRC).

Fig. 2. Location of the test site.

Fig. 3. Test layout.

Fig. 4. The layout of subsurface deformation monitoring.

Fig. 5. Water level variation.

(a) Distribution of water level on Aug. 15

(b) Distribution of water level recovery on Aug. 30

Fig. 6. The variation of surface settlement distribution during the pumping.

(a) Aug. 10, 2018

(b) Aug. 15, 2018

Fig. 7. The variation of surface settlement distribution after the pumping.

(a) Aug 24, 2018

(b) Sep. 11, 2018

(c) Nov. 17, 2018

(d) Jan. 16, 2019

Fig. 8. Contour plot of the subsurface strain field.

(a) During the pumping

(b) After the pumping

Fig. 9. Ground deformation trends and fitted curves of borehole D1.

Fig. 10. Settlement distribution along the metro line.

Fig. 11. The minimum curvature radius of typical sections along the metro line.

Figures

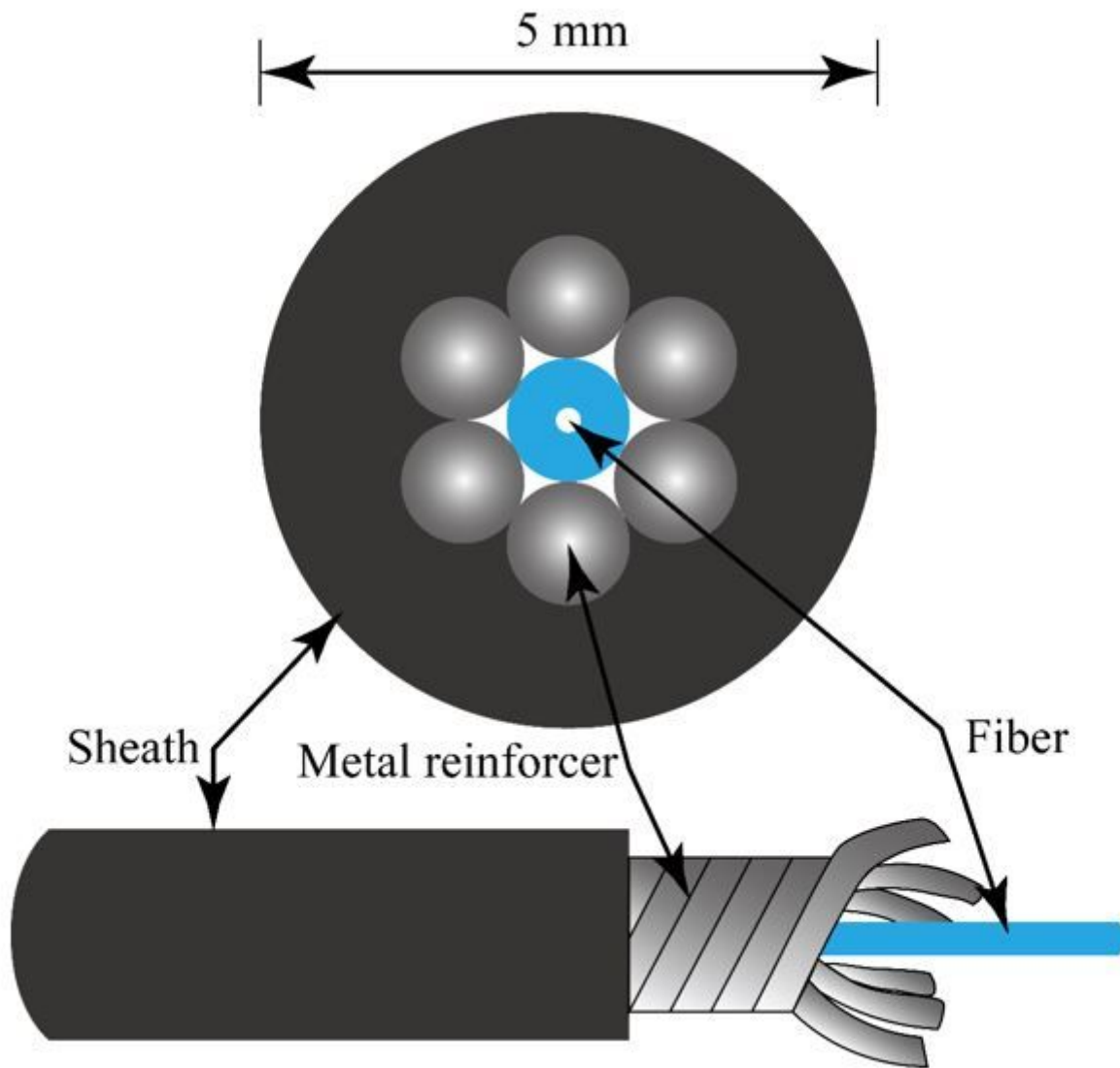


Figure 1

The structure of a metal-reinforced single-core cable (MRC).



Figure 2

Location of the test site. Note: The designations employed and the presentation of the material on this map do not imply the expression of any opinion whatsoever on the part of Research Square concerning the legal status of any country, territory, city or area or of its authorities, or concerning the delimitation of its frontiers or boundaries. This map has been provided by the authors.

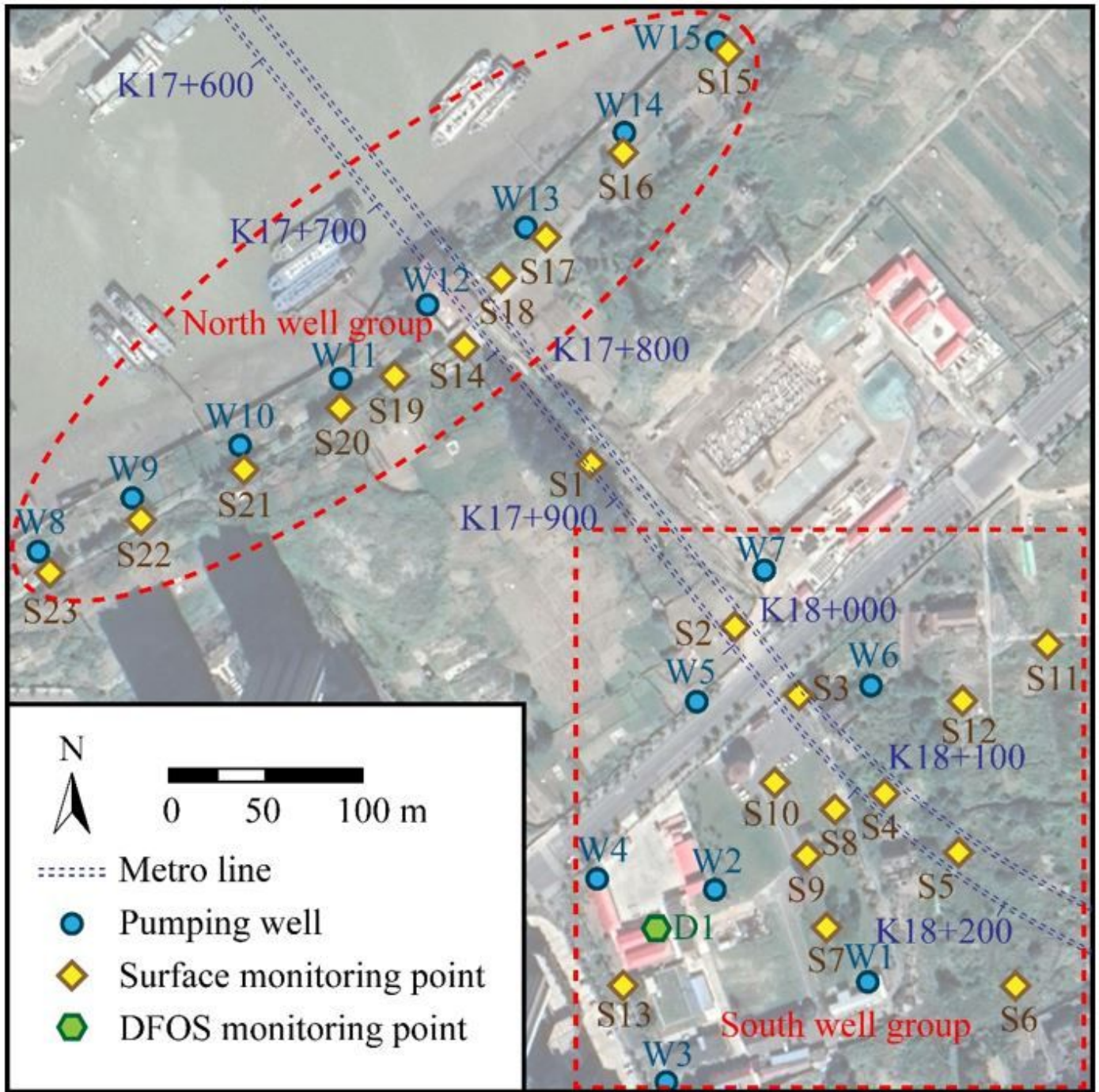


Figure 3

Test layout. Note: The designations employed and the presentation of the material on this map do not imply the expression of any opinion whatsoever on the part of Research Square concerning the legal status of any country, territory, city or area or of its authorities, or concerning the delimitation of its frontiers or boundaries. This map has been provided by the authors.

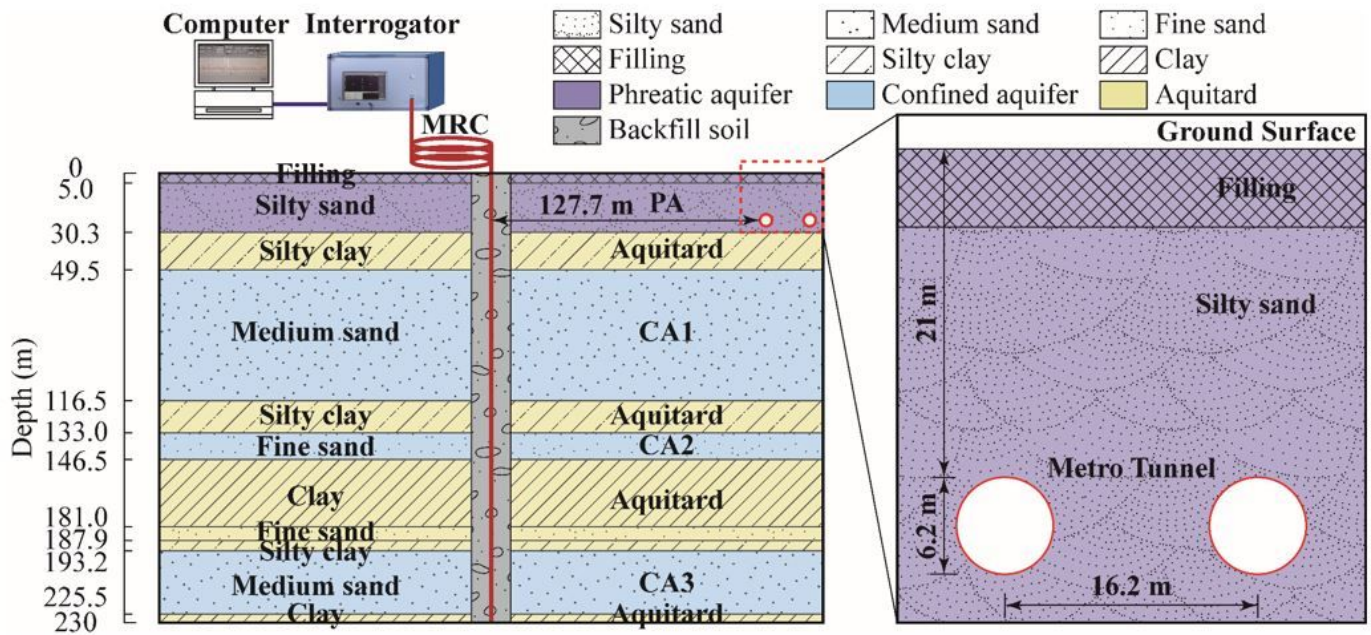


Figure 4

The layout of subsurface deformation monitoring.

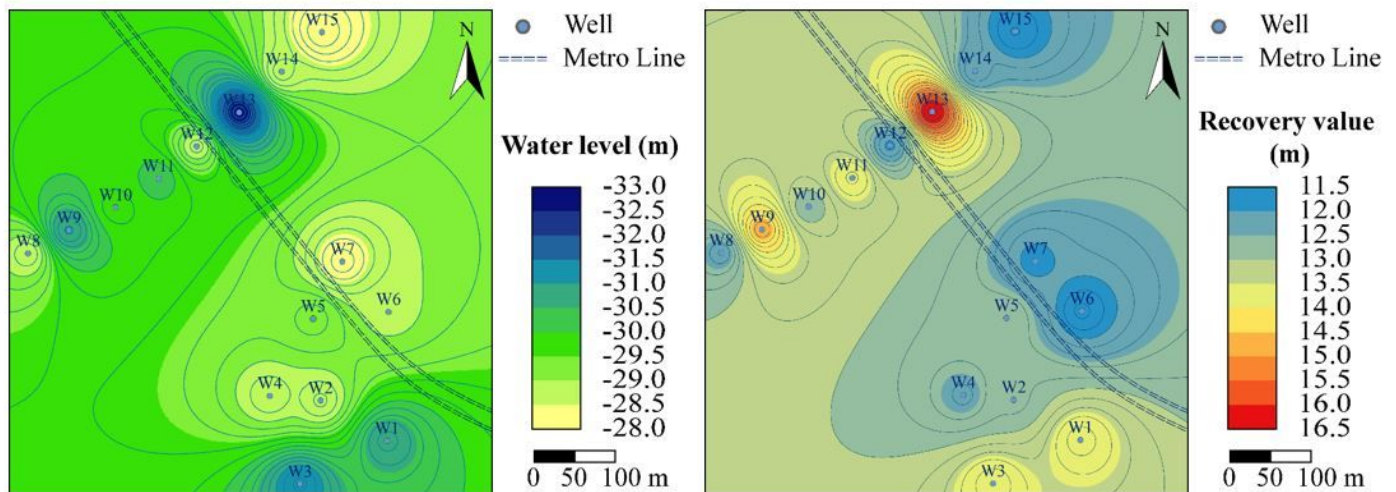


Figure 5

Water level variation. (a) Distribution of water level on Aug. 15; (b) Distribution of water level recovery on Aug. 30. Note: The designations employed and the presentation of the material on this map do not imply the expression of any opinion whatsoever on the part of Research Square concerning the legal status of any country, territory, city or area or of its authorities, or concerning the delimitation of its frontiers or boundaries. This map has been provided by the authors.

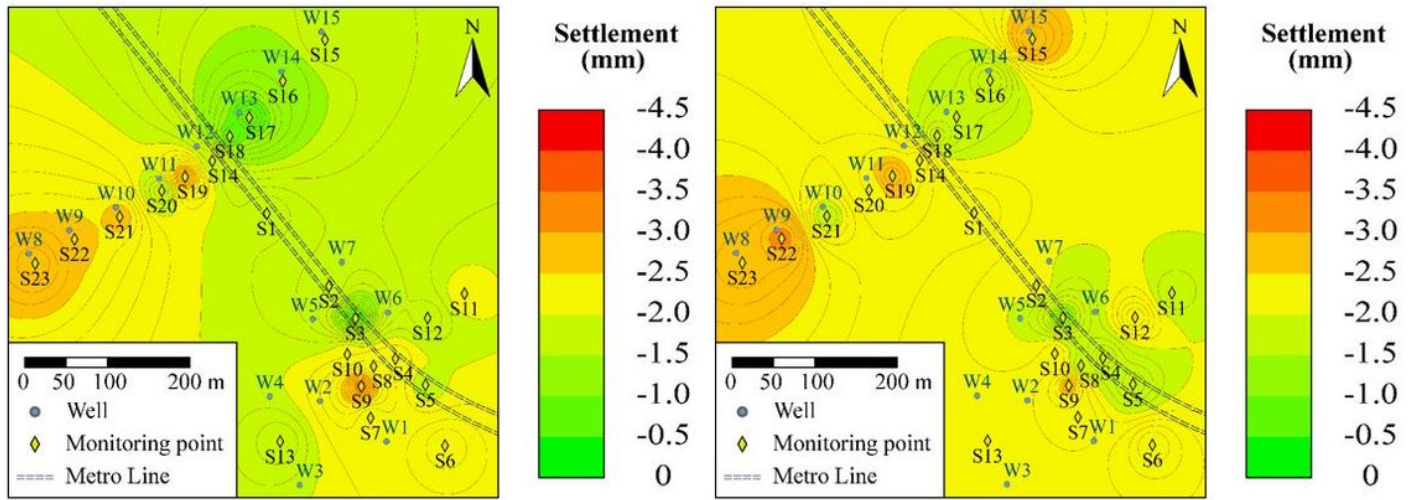


Figure 6

The variation of surface settlement distribution during the pumping. (a) Aug. 10, 2018; (b) Aug. 15, 2018. Note: The designations employed and the presentation of the material on this map do not imply the expression of any opinion whatsoever on the part of Research Square concerning the legal status of any country, territory, city or area or of its authorities, or concerning the delimitation of its frontiers or boundaries. This map has been provided by the authors.

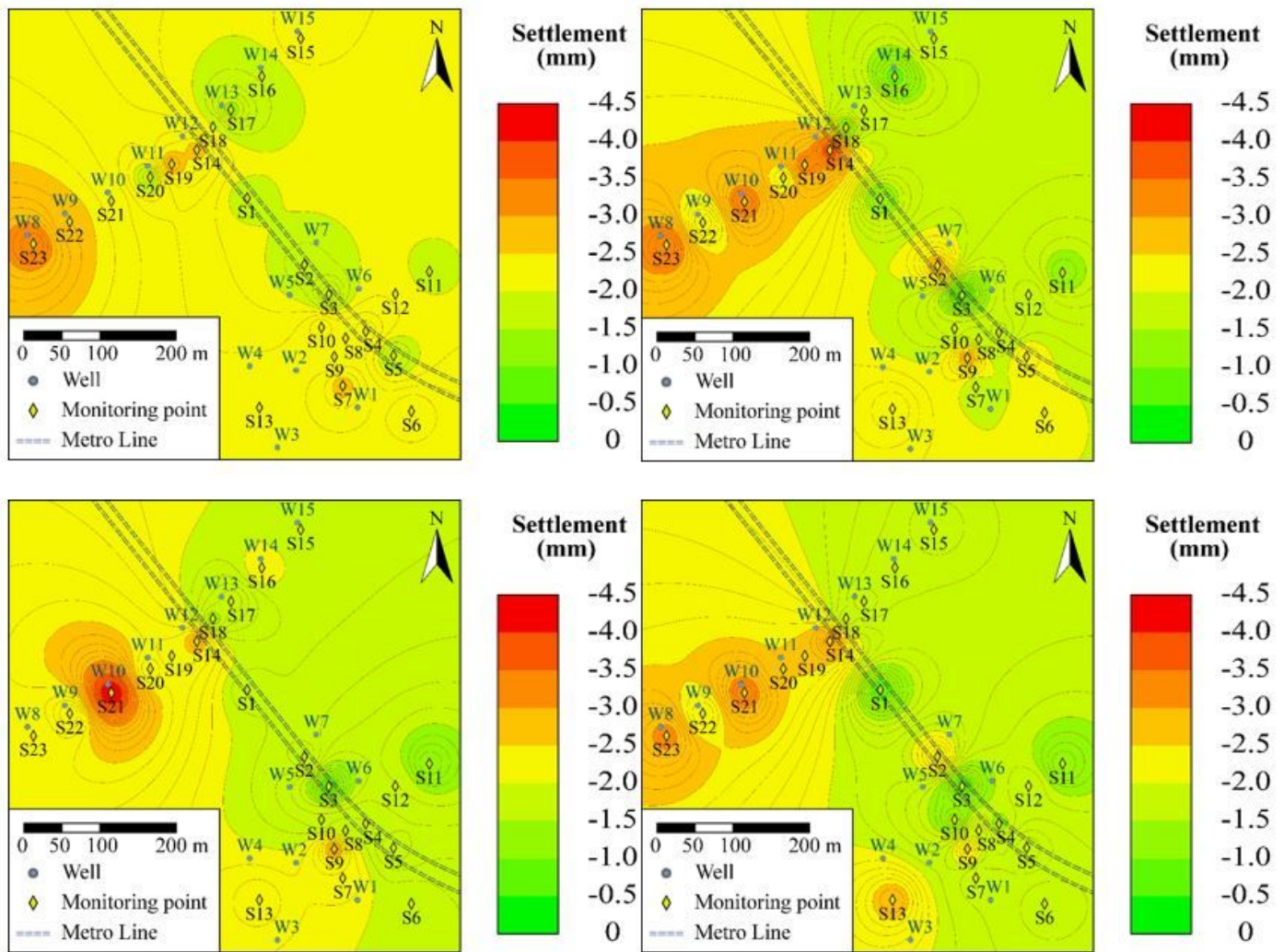


Figure 7

The variation of surface settlement distribution after the pumping. (a) Aug 24, 2018; (b) Sep. 11, 2018; (c) Nov. 17, 2018; (d) Jan. 16, 2019. Note: The designations employed and the presentation of the material on this map do not imply the expression of any opinion whatsoever on the part of Research Square concerning the legal status of any country, territory, city or area or of its authorities, or concerning the delimitation of its frontiers or boundaries. This map has been provided by the authors.

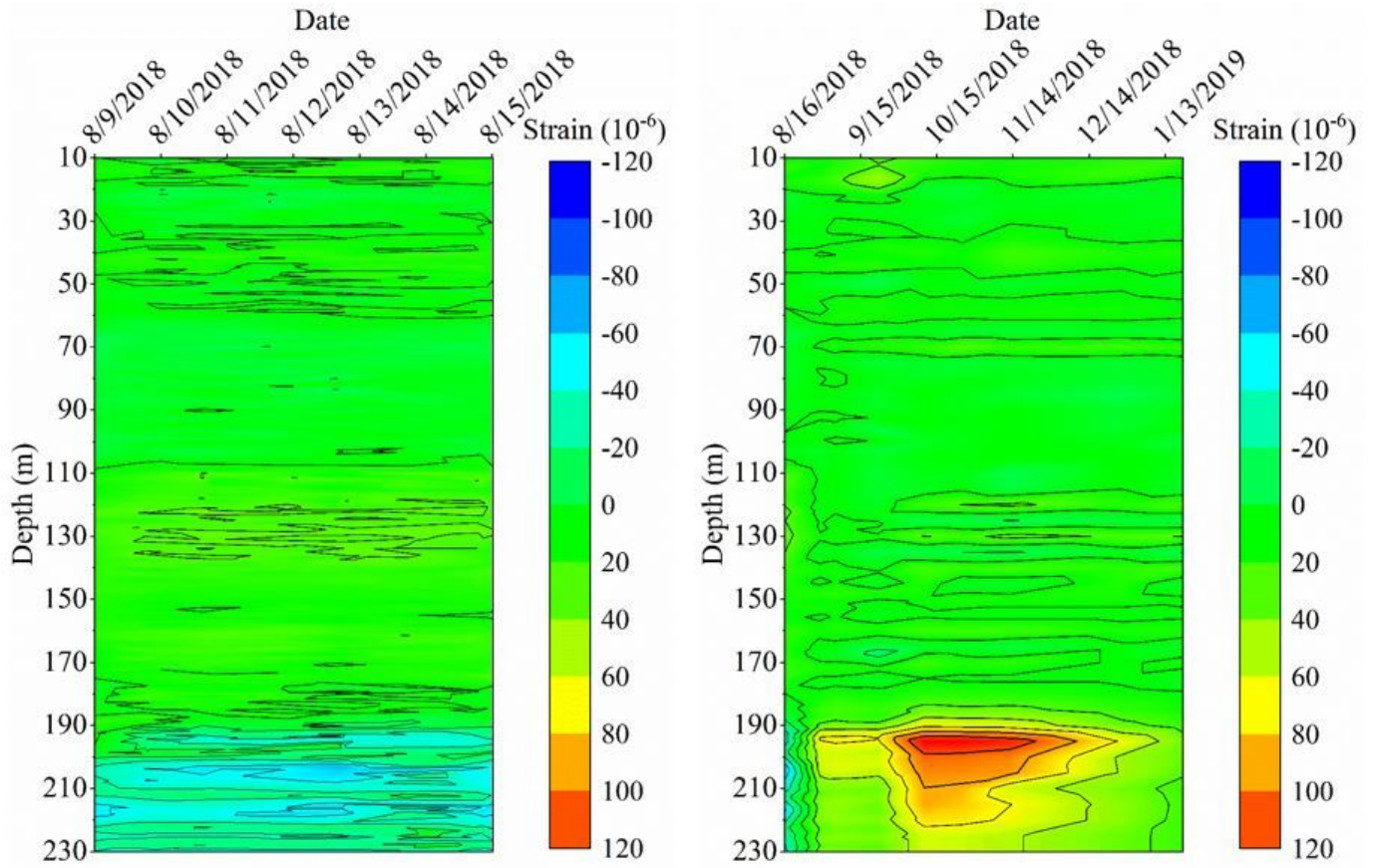


Figure 8

Contour plot of the subsurface strain field. (a) During the pumping; (b) After the pumping.

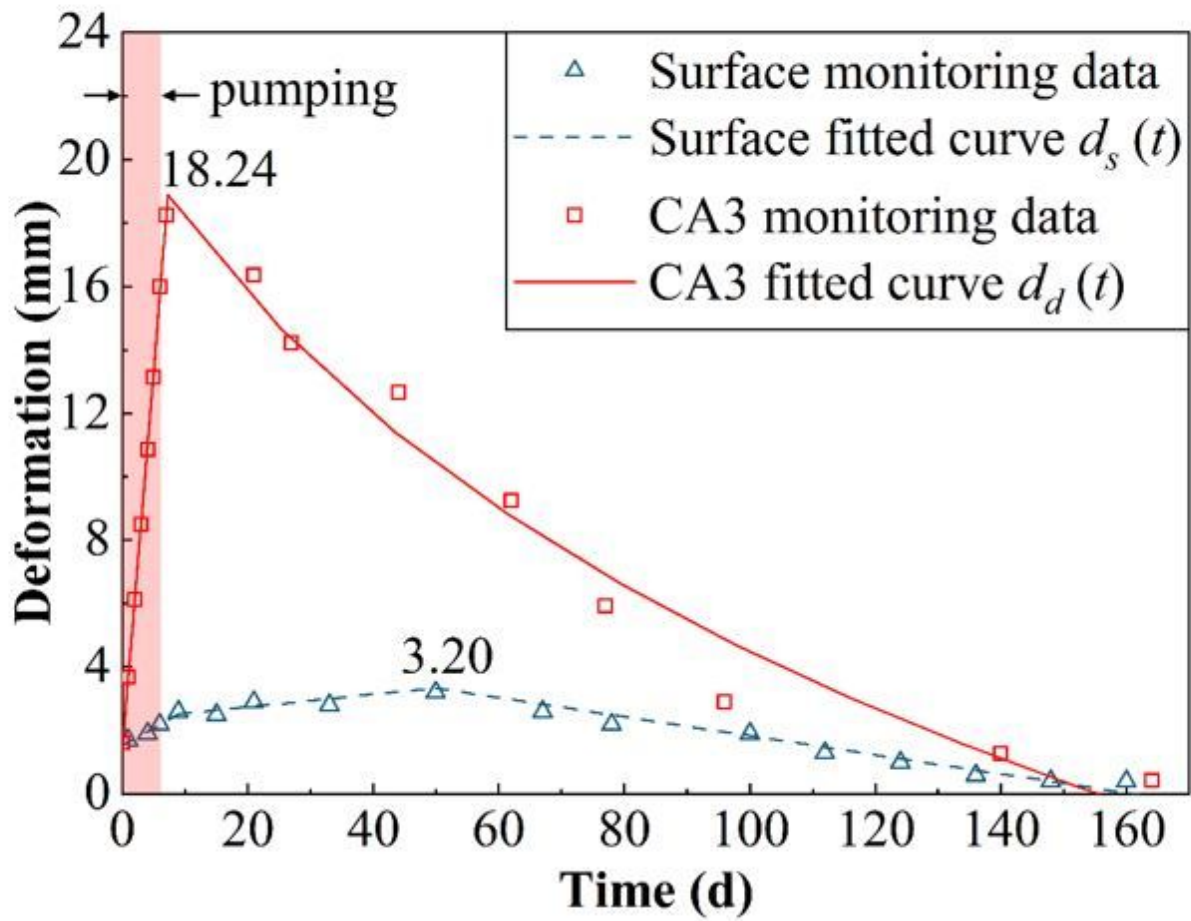


Figure 9

Ground deformation trends and fitted curves of borehole D1.

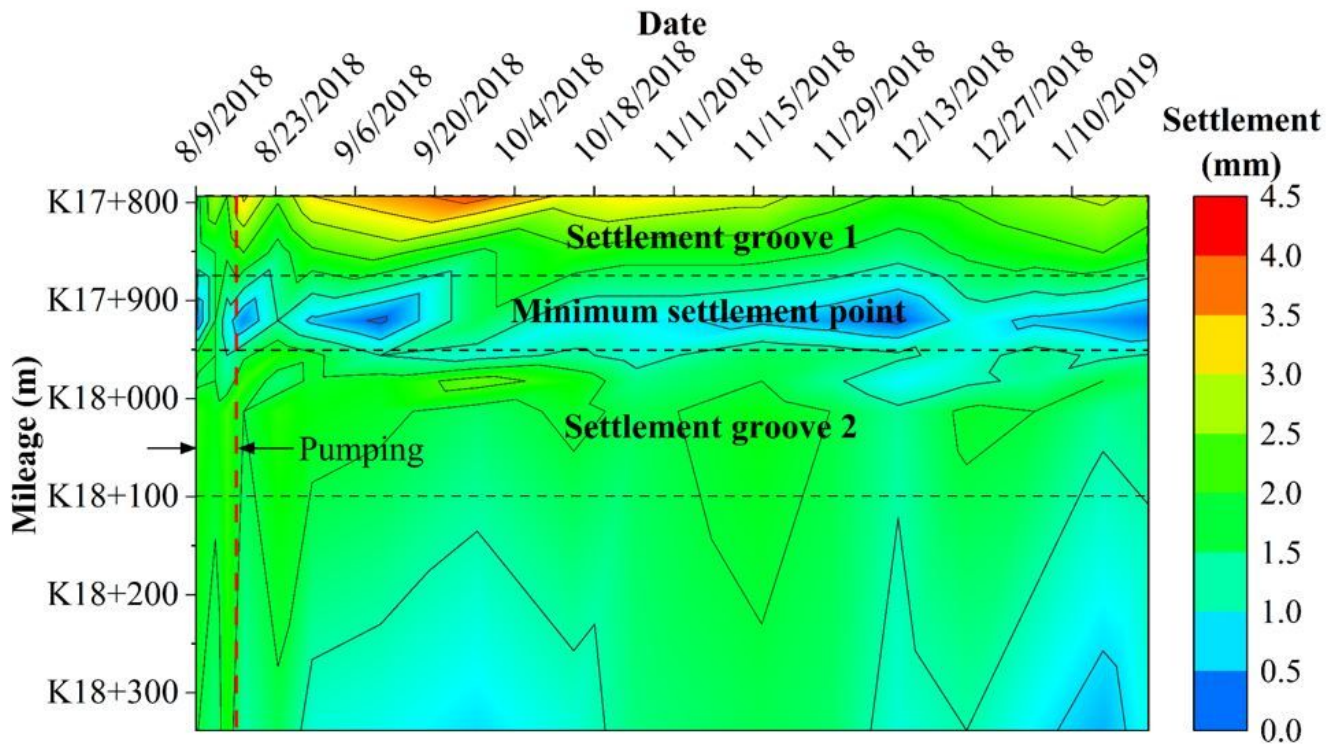


Figure 10

Settlement distribution along the metro line.

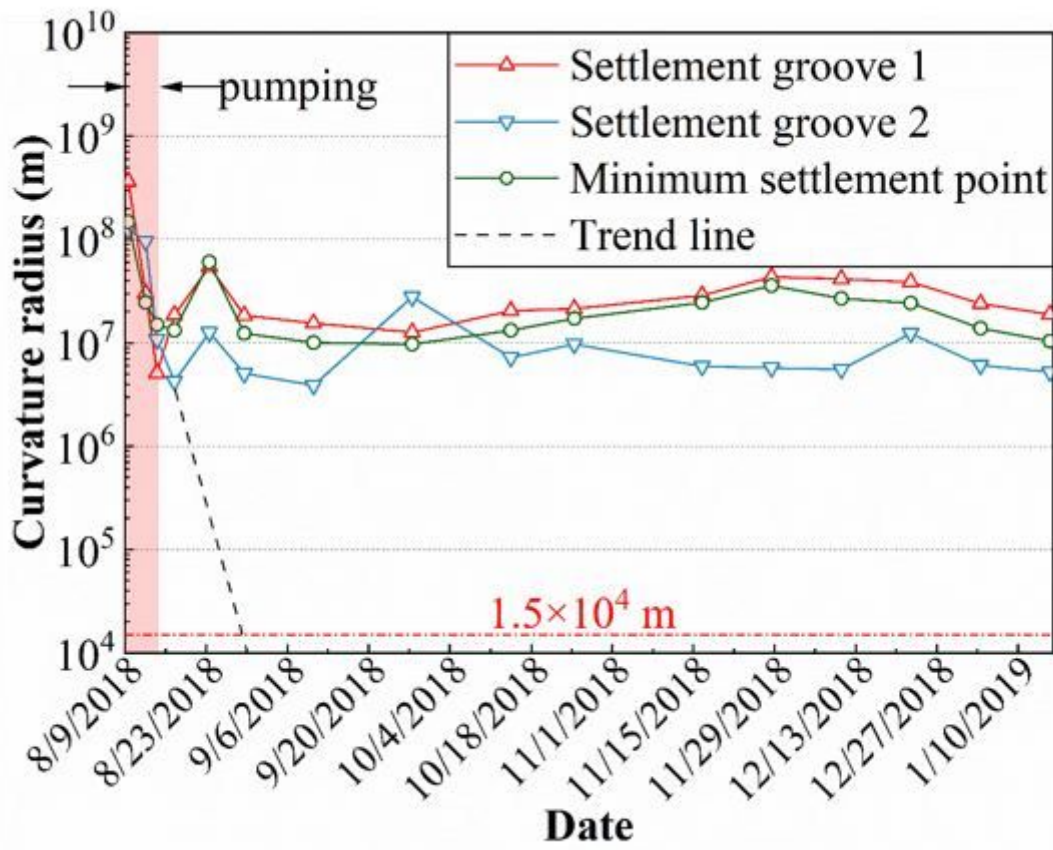


Figure 11

The minimum curvature radius of typical sections along the metro line.